

# High temperature surface state in Kondo insulator $U_3Bi_4Ni_3$

Christopher Broyles,<sup>1</sup> Xiaohan Wan,<sup>2</sup> Wenting Cheng,<sup>2</sup> Dingsong Wu,<sup>3</sup> Hengxin Tan,<sup>4</sup> Qiaozhi Xu,<sup>1</sup> Shannon L. Gould,<sup>1</sup> Hasan Siddiquee,<sup>1</sup> Leyan Xiao,<sup>1</sup> Ryan Chen,<sup>1</sup> Wanyue Lin,<sup>1</sup> Yuchen Wu,<sup>1</sup> Prakash Regmi,<sup>5</sup> Yun Suk Eo,<sup>5</sup> Jieyi Liu,<sup>6</sup> Yulin Chen,<sup>3,7</sup> Binghai Yan,<sup>4,8,\*</sup> Kai Sun,<sup>2,†</sup> and Sheng Ran<sup>1,‡</sup>

<sup>1</sup>*Department of Physics, Washington University in St. Louis, St. Louis, MO 63130, USA*

<sup>2</sup>*Department of Physics, University of Michigan, Ann Arbor, MI 48109, USA*

<sup>3</sup>*Department of Physics, University of Oxford, Oxford OX1 3PU, United Kingdom*

<sup>4</sup>*Department of Condensed Matter Physics,  
Weizmann Institute of Science, Rehovot 7610001, Israel*

<sup>5</sup>*Department of Physics and Astronomy,  
Texas Tech University, Lubbock, TX 79409, USA*

<sup>6</sup>*Diamond Light Source, Didcot OX11 0DE, United Kingdom*

<sup>7</sup>*ShanghaiTech Laboratory for Topological Physics,  
Shanghai 200031, People's Republic of China*

<sup>8</sup>*Department of Physics, The Pennsylvania State University, University Park, PA 16802, USA*

(Dated: February 6, 2025)

## Abstract

The resurgence of interest in Kondo insulators has been driven by two major mysteries: the presence of metallic surface states and the observation of quantum oscillations. To further explore these mysteries, it is crucial to investigate another similar system beyond the two existing ones,  $SmB_6$  and  $YbB_{12}$ . Here, we address this by reporting on a Kondo insulator,  $U_3Bi_4Ni_3$ . Our transport measurements reveal that a surface state emerges below 250 K and dominates transport properties below 150 K, which is well above the temperature scale of  $SmB_6$  and  $YbB_{12}$ . At low temperatures, the surface conductivity is about one order of magnitude higher than the bulk. The robustness of the surface state indicates that it is inherently protected. The similarities and differences between  $U_3Bi_4Ni_3$  and the other two Kondo insulators will provide valuable insights into the nature of metallic surface states in Kondo insulators and their interplay with strong electron correlations.

---

\* Corresponding author: [binghai.yan@weizmann.ac.il](mailto:binghai.yan@weizmann.ac.il)

† Corresponding author: [sunkai@umich.edu](mailto:sunkai@umich.edu)

‡ Corresponding author: [rans@wustl.edu](mailto:rans@wustl.edu)

## I. INTRODUCTION

In Kondo lattice materials, interactions between conduction electrons and localized  $f$  electrons lead to the screening of localized magnetic moments, generating a spin-scattering resonance state and a hybridization gap (1–5). If the Fermi energy lies within the hybridization gap, the system is a Kondo insulator (6). Two well-known examples are  $\text{SmB}_6$  and  $\text{YbB}_{12}$ , both of which exhibit a curious phenomenon: the saturation of electrical resistivity at low temperatures (7, 8). This resistivity saturation is particularly well-documented in  $\text{SmB}_6$  and has been the focus of extensive study for decades due to the mystery it presents (9). In a conventional insulator, resistivity should increase as temperature decreases, but in these materials, it unexpectedly plateaus, indicating an unusual form of conduction. Various theories, such as impurity states or in-gap states, have been proposed to explain this behavior (10–12). In the past decade, a hypothesis has emerged suggesting that the resistivity saturation in  $\text{SmB}_6$ , and potentially in  $\text{YbB}_{12}$ , might be due to the presence of metallic surface states of topological origin (13–18). This idea has sparked substantial interest and is supported by numerous experimental studies, though some results show inconsistencies with a purely topological interpretation (19–22). The exact cause of the resistivity saturation and the full nature of the surface states in  $\text{SmB}_6$  and  $\text{YbB}_{12}$  remain subjects of active investigation.

In addition to the mystery of resistivity saturation, both  $\text{SmB}_6$  and  $\text{YbB}_{12}$  exhibit another intriguing phenomenon: the observation of quantum oscillations (23–30). Typically, quantum oscillations are associated with a Fermi surface in metals, making their presence in these insulating materials particularly surprising. These oscillations suggest that  $\text{SmB}_6$  and  $\text{YbB}_{12}$  might host unconventional excitations, such as neutral fermions or other exotic states (23, 24, 26, 27), that challenge the theoretical understanding of a Kondo insulating state (31–39). While metallic surface states have been proposed as a possible explanation, they do not fully account for the quantum oscillations, as these oscillations appear to originate from the bulk of the material. Nevertheless, the fact that both  $\text{SmB}_6$  and  $\text{YbB}_{12}$  exhibit both resistivity saturation and quantum oscillations suggests that these two phenomena may be related in some way, even if the underlying mechanisms are different.

Given the unresolved mysteries surrounding  $\text{SmB}_6$  and  $\text{YbB}_{12}$ , discovering another Kondo insulator that exhibits similar phenomena at a different energy scale would be invaluable. Uranium-based Kondo lattice systems present a promising platform for such discoveries, as the stronger hybridization between U  $5f$  electrons and conduction electrons can result in a considerably higher hybridization

gap and Kondo temperature compared to their rare-earth counterparts (40–42). To this end, we identified a potential candidate:  $\text{U}_3\text{Bi}_4\text{Ni}_3$ . It crystallizes onto a cubic lattice with non-centrosymmetric symmetry in the space group I-43d (No. 220) (43), isostructural to the Ce-based Kondo insulator  $\text{Ce}_3\text{Bi}_4\text{Pt}_3$  (Fig.1a). Upon cooling below  $T_K = 100$  K, there is a suppression of magnetic susceptibility (43) and an increase of correlation between  $5f$  and conduction electrons (44), both are signatures of Kondo screening of the uranium local moments. The hybridization gap was measured using photoemission spectroscopy (43), revealing a gap of 72 meV, while NQR  $T_1^{-1}$  spin-lattice relaxation time measurements (44) found a smaller gap of 19 meV. In this work, we provide conclusive evidence of metallic surface state of  $\text{U}_3\text{Bi}_4\text{Ni}_3$  that emerges below 250 K, dominating the transport properties below 150 K. This high-temperature, surface-dominated conduction in a Kondo insulator is unprecedented and could consequentially advance our understanding of the fundamental physics underlying metallic surface states in strongly correlated systems.

## II. RESULTS

### A. Kondo insulating ground state

First we characterize the Kondo insulator behaviour of  $\text{U}_3\text{Bi}_4\text{Ni}_3$ . At high temperatures, the magnetic susceptibility,  $M/H$ , shows a Curie-Weiss temperature dependence, fitting to a magnetic moment of  $3.68 \mu_B$  and  $T_{CW} = -162$  K (Fig. 1b). Below 100 K, a signature of Kondo screening emerges, with  $M/H$  saturating to a value near  $8 \cdot 10^{-3}$  emu/Oe- $\text{U}_{\text{mol}}$ . This is consistent with an NMR/NQR study (44), which demonstrated a breakdown of the scaling between the Knight shift and magnetic susceptibility below 100 K. The field dependent magnetization,  $M(H)$ , reveals no ferromagnetic magnetic ordering or field induced magnetic transition, with linear scaling for  $5 \text{ K} \leq T \leq 300 \text{ K}$  (Fig.1c).

The longitudinal resistivity ( $\rho_{xx}$ ) resembles that of a narrow gap semiconductor at room temperature, with  $\Delta = 95$  meV (Fig.1d). This gap size is appreciably larger than those observed in  $\text{SmB}_6$  and  $\text{YbB}_{12}$  (45–49). As the temperature is lowered past the Kondo temperature ( $T_K \approx 100$  K),  $\rho_{xx}$  flattens around 185 milli-ohm-cm, before an additional increase below 50 K, leading to a saturation at 290 milli-ohm-cm. An Arrhenius fit for  $30 \text{ K} \leq T \leq 60 \text{ K}$  gives an activation gap of  $\Delta = 1.5$  meV. This temperature dependence could be consistent with Kondo hybridization renormalizing and reducing  $\Delta$  below 100 K; however, the low temperature saturation in  $\rho_{xx}$  is more than an order of magnitude larger than previously reported (43).

The magneto-transport measurements, displayed in Figure 1e-g, provide further support of the Kondo coherent ground-state. The high temperature Hall resistivity ( $\rho_{xy}$ ) exhibits a sigmoid-like shape, which can not be accurately represented by a simple two-band model and is typically indicative of the anomalous Hall effect (AHE) (50). The anomalous Hall is most clearly seen at 150 K, with a distinct, sharp jump near zero magnetic field. By incorporating a constant into the two band Hall model (51),  $\rho_{xy}^{\text{AHE}}$  is extracted and the temperature dependence is plotted in Figure 1h. The anomalous Hall contribution gradually increases from room temperature to 150 K, after which it begins to decrease. This overall temperature dependence of the anomalous Hall effect is consistent with what has been observed in other Kondo lattice systems (52). Above the Kondo temperature, incoherent Kondo scattering dominates the transport properties. A modest magnetic field can polarize the local moments, leading to the anomalous Hall effect through a scattering mechanism (52, 53). As the temperature decreases, a smaller magnetic field is needed to polarize the local moments; thus, the curve narrows and transitions into a sharp, step-like shape at 150 K. In the meantime, Kondo scattering logarithmically increases with the decreasing temperature, enhancing the anomalous Hall effect (54, 55). Once Kondo scattering becomes coherent below  $T_K$ , the anomalous Hall gradually decreases. Note that below 50 K, the anomalous Hall contribution becomes negligible and the Hall data fits equally well with a pure two-band model.

To further confirm the Kondo ground state of  $\text{U}_3\text{Bi}_4\text{Ni}_3$ , we performed angle-resolved photoemission spectroscopy (ARPES) measurements at  $T = 20$  K. To highlight the spectral profile of U 5*f* character, we used 98 eV photon energy, which resonantly enhances the photoionization cross section of U 5*f* states. Figure 2 presents the energy spectra for the resonant condition at 98 eV, and the off-resonant condition at 92 eV for comparison. While both spectra show a strong maximum at -2 eV, indicative of a flat band, the resonant enhanced band image maintains a strong intensity until  $E_F$ . The integrated energy distribution curve (EDC) reveals a refined structure near the Fermi level, with two peaks within 300 meV of  $E_F$  (indicated by red arrows). These weak peaks indicate U 5*f* multiplet states, which participate in the many-body Kondo resonance, as seen in other uranium-based Kondo lattice systems (56, 57). The EDC of both 98 and 92 eV is suppressed at Fermi energy, indicating the insulating nature. The suppressed overall intensity at the Fermi level and the enhanced U 5*f* spectral weight near the Fermi energy in the resonant spectrum are consistent with a Kondo insulator, similar to observations in  $\text{SmB}_6$  and  $\text{YbB}_{12}$  (20, 58, 59).

## B. Metallic surface state

The temperature dependent resistivity of  $\text{U}_3\text{Bi}_4\text{Ni}_3$  exhibits a plateau below 150 K, shown in Fig. 1d. Similar plateaus have been observed in both  $\text{SmB}_6$  (7) and  $\text{YbB}_{12}$  (8), indicative of either a metallic surface state or extended in-gap states. To identify the origin of the plateau, we performed a thickness dependant study. The sample was successively polished to 150  $\mu\text{m}$  and 120  $\mu\text{m}$ . Above 200 K, the resistivity is essentially independent of thickness, which is a clear indication of bulk transport (Fig. 1d). In contrast, at low temperatures the resistivity markedly decreases as the thickness is reduced. This reduction suggests that the resistance no longer scales linearly with thickness, a clear sign of surface charge transport.

In order to more accurately determine the bulk and surface transport coefficients, we employ a non-local transport measurement, with the inverted resistance setup (60). The inverted transport measurement makes use of the Corbino-disk geometry depicted in Figure 3a, where electrode 2 acts as a two-dimensional Faraday cage for the surface area enclosed by this electrode. This technique has been reliably used to decouple the surface and the bulk conduction channels of  $\text{SmB}_6$  and other strongly correlated insulators (61, 62). Within this setup, we can measure two distinct four-terminal resistances:  $R_{12;12}$  and  $R_{12;34}$ , where the first pair of indices denotes the current-carrying electrodes, and the second pair represents the voltage-measuring electrodes. For bulk-dominated transport, both  $R_{12;12}$  and  $R_{12;34}$  are proportional to the bulk resistivity. Conversely, in the scenario where surface transport dominates,  $R_{12;12}$  and  $R_{12;34}$  will show distinctly different dependencies on surface and bulk resistivity. This distinction arises because, when current is introduced between electrodes (1) and (2), charge carriers traverse parallel paths from  $1 \rightarrow 2$  and  $1 \rightarrow 3 \rightarrow 4 \rightarrow 2$ , leveraging the enhanced conductivity of the surface. Therefore, in cases of surface-dominant transport,  $R_{12;12}$  is directly proportional to the surface resistivity ( $R_{12;12} \propto \rho_s$ ), while  $R_{12;34}$  receives mixed contributions from both bulk and surface resistivity and exhibits a scaling behavior characterized by an inverse-gap dependence, (i.e.,  $R_{12;34} = C t \frac{\rho_s^2}{\rho_b} \propto \text{Exp}[-\frac{\Delta}{k_B T}]$ ) (60), where 'C' is a constant, 't' is the sample thickness, ' $\rho_s$ ' is the surface resistivity, ' $\rho_b$ ' is the bulk resistivity, ' $\Delta$ ' is the energy gap, ' $k_B$ ' is the Boltzmann constant, and 'T' is the temperature. The inverse-gap behaviour is explained in more details in SI.

Multiple  $\text{U}_3\text{Bi}_4\text{Ni}_3$  samples were polished to a thickness ranging between 130 and 210  $\mu\text{m}$ , and the Corbino disk electrodes were patterned on top and bottom faces. Here we present two Corbino-disk

samples in Figure 3, which have been measured in the  $R_{12;12}$  and  $R_{12;34}$  configurations. The  $R_{12;12}$  configuration has similar behavior to  $\rho_{xx}(T)$ , but only saturates at  $R(5K)/R(400K) \approx 10$  (Fig. 3b,c). When measured in the  $R_{12;34}$  configuration, the peak values reaches roughly 10 before the insulator-metal crossover. To compare the activated scaling, Arrhenius fittings were applied between 200 K and 300 K, revealing a gap ranging from 78.8 – 82.8 meV and 56.5 – 74.7 meV for  $R_{12;34}$  and  $R_{12;12}$  respectively. Below the surface state onset,  $R_{12;34}$  displays a dual inverse-gap behavior. The initial gap has values ranging from  $\Delta_{\text{low}}^1 = 17.7 - 39.3$  meV and transitions to a much smaller gap of  $\Delta_{\text{low}}^2 = 2.4-3.1$  meV. At low temperatures, sample 1 (S1) has a rise in  $R_{12;34}$  around 25 K. The variety of these surface transport features demonstrates the robust nature of the surface state to carrier doping and impurities that characterize the sample variation.

The use of finite element analysis (FEA) allows the separation of the bulk and surface transport properties. We conducted simulations of the charge transport using a geometry that mirrors the experimental setup. By employing the bulk resistivity ( $\rho_b$ ) and surface conductivity ( $\sigma_s$ ) as fitting parameters, we compare the simulated outcome with the experimental values of  $R_{12;12}$  and  $R_{12;34}$ . This allowed us to extract the fitted values of  $\rho_b$  and  $\sigma_s$  at varying temperatures. The results of these fittings are displayed in Figure 3d-i. The bulk resistivity of S1 is plotted versus  $T^{-1}$  in Figure 3d, which shows an activation gap of 97.4 meV above 150 K and a much smaller activation gap of 3.2 meV below  $T_K = 100$  K. As the temperature drops below 30 K,  $\rho_b$  saturates, likely due to the contribution of an impurity band or other in-gap state at low temperatures. The surface conductivity of S1 markedly increases from 250 K and exhibits nearly temperature independent behavior below 150 K. The ratio of  $\sigma_b * t / \sigma_s$  reaches unity at 150 K, marking a crossover in the transport properties, which is just below the peak in  $R_{12;34}$  at 180 K (Fig. 3f). At the lowest temperature,  $\sigma_s$  is roughly 5 times larger than the bulk, which is remarkable for a bulk thickness of  $t = 210 \mu\text{m}$ .

The sample variation of the surface state is highlighted in the FEA of Corbino-disk sample 2 (S2). The low temperature bulk gap is comparable at  $\Delta = 4.2$  meV, but  $\sigma_b$  continues to decrease with temperature (Fig. 3g). Likewise,  $\sigma_s$  keeps increasing below 120 K, rather than reaching a temperature independent value (Fig. 3h). Due to the large conductivity of the bulk, the ratio of  $\sigma_b * t / \sigma_s$  does not reach unity until 50 K (Fig. 3i). However, at base temperature, surface conductivity reaches 10 times that of the bulk.

### III. DISCUSSION

Our discovery of a metallic surface state in  $U_3Bi_4Ni_3$  is particularly important because, to our knowledge, it represents the only other example of such a state in a Kondo insulator besides  $SmB_6$  and  $YbB_{12}$ . All three materials exhibit similar electron transport characteristics: activated behavior at high temperatures and resistivity saturation at low temperatures, although the bulk resistivity of  $SmB_6$  is a few orders of magnitude higher than that of  $U_3Bi_4Ni_3$  (61, 62). What makes  $U_3Bi_4Ni_3$  more intriguing is that its surface state emerges at a much higher temperature. The similarities and differences between  $U_3Bi_4Ni_3$  and these well-studied Kondo insulators may shed light on the mechanisms underlying metallic surface states in these materials.

One key similarity across these materials is the exceptional robustness of the surface state. In our study, surface-dominated transport has been universally observed across all samples and surfaces of  $U_3Bi_4Ni_3$ , suggesting that the surface state is exceptionally robust and unaffected by surface conditions and impurities, similar to  $SmB_6$  (61, 62). This robustness is further emphasized by the fact that the surface state of  $U_3Bi_4Ni_3$  remains dominant over a wide temperature range, achieving conductivity levels one order of magnitude higher than the bulk, despite variations in bulk conductivity that may indicate the presence of impurity bands in the bulk. This resilience is notable, especially considering that the surfaces have been exposed to air and contaminants during the polishing process.

This behavior is reminiscent of  $SmB_6$ , where non-stoichiometrically grown samples exhibit flattening of inverted resistance at low temperatures due to bulk impurities (61). However, in both materials, the surface state remains dominant, indicating a level of resilience that is unusual for trivial surface states, which typically lack such robustness and may arise only under specific conditions. This resilience suggests that the surface states in  $U_3Bi_4Ni_3$ , like those in  $SmB_6$ , may be inherently protected. Among the known mechanisms for robust surface states, topological band inversion stands out as the most plausible origin for such persistent surface conductivity. However, due to Kondo hybridization, simple DFT+U calculations may not be able to capture the electronic structure of  $U_3Bi_4Ni_3$  (see SI). In addition, unlike  $SmB_6$  and  $YbB_{12}$ , which have inversion symmetry and thus enable a straightforward determination of band topology at high-symmetry points without any detailed knowledge of the bands (63),  $U_3Bi_4Ni_3$  lacks inversion symmetry. As a result, establishing its topological index requires a detailed understanding of the Bloch states throughout the entire Brillouin zone. This heightened sensitivity means that even minor inaccuracies in the calculated band structure can lead to significantly

incorrect conclusions about its topological nature. More advanced methods, such as DMFT, are needed to fully understand the topology of  $U_3Bi_4Ni_3$ .

Despite these similarities, there are notable differences in the energy scales at which these surface states emerge, when comparing  $U_3Bi_4Ni_3$  with  $SmB_6$  and  $YbB_{12}$ . In  $SmB_6$ , the onset of Kondo hybridization begins at 60-90 K and the full coherence is established below 30-40 K (47, 48). The surface state, emerging at 4 K, arises from the Kondo ground-state (64, 65). Similarly,  $YbB_{12}$  has a Kondo temperature of 200 K (49, 66), but the resistivity saturation does not happen until below 2 K (8). In contrast, the surface state of  $U_3Bi_4Ni_3$  appears above the Kondo temperature: the emergence of the surface state has a concrete temperature scale between 200 - 250 K, while the Kondo energy scale is set at around  $T_K = 100$  K.

The observation of a surface state emerging at temperatures above the Kondo temperature raises important questions about the origin of the surface state in  $U_3Bi_4Ni_3$ . One possibility is that a robust, protected surface state already exists at high temperatures, potentially associated with a topological gap. Upon cooling through the Kondo temperature, the gap is renormalized and reduced in size, but the fundamental nature of the surface state remains unchanged. This interpretation is supported by the absence of gap closure throughout the entire temperature range, suggesting that the topology remains consistent through the Kondo coherence process, as a change in topology would typically require the closing and reopening of a gap. The dual-gap features observed in both standard and inverted resistance transport, as well as in the bulk conductivity revealed through FEA, are also consistent with the gap renormalization by the Kondo hybridization. In this scenario, there is a crossover between a topological insulator (TI) and a Kondo topological insulator (KTI), which are smoothly connected without any phase boundary. One phase containing both TI region and KTI region and a adiabatic continuity between the two region is an interesting theory conjecture that requires further investigated in the future. An important question is whether the Kondo mechanism can still operate within an insulating phase. In principle, Kondo physics relies on hybridization between conduction and localized electrons, which typically requires a well-defined Fermi surface. However, this apparent contradiction can be reconciled if we consider a strongly correlated insulating state. At high temperatures, strong localization mechanisms dominate, suppressing electron mobility. As the temperature decreases, electron coherence improves, allowing some electrons to become sufficiently delocalized to screen local moments. In this way, Kondo behavior can emerge even within an ostensibly insulating phase.

Alternatively, the surface state observed at high temperatures might not be due to a topological gap,

but instead arise from a trivial origin, only becoming protected as the material transitions into the Kondo insulator state upon cooling. Our data do not provide definitive answers to distinguish between the two, and further investigation is needed to determine which mechanism—or combination of mechanisms—best explains the metallic surface state in  $\text{U}_3\text{Bi}_4\text{Ni}_3$ . Regardless, this behavior highlights the intricate relationship between Kondo physics and surface states, making  $\text{U}_3\text{Bi}_4\text{Ni}_3$  an important system for understanding the fundamental physics governing metallic surface states in strongly correlated materials.

Regardless of their precise nature, the surface states observed in  $\text{U}_3\text{Bi}_4\text{Ni}_3$  present a novel example of a robust, two-dimensional (2D) electron gas system. The interplay of Kondo physics within these 2D surface states introduces strong electron correlations and pronounced spin-orbit coupling, which is anticipated to exceed that of other well-studied 2D gases, such as semiconductor interfaces, graphene and transition metal dichalcogenides. Moreover, these surface states exhibit high conductivity and mobility, with sheet conductivity at 5 K reaching  $0.1\text{-}0.5\text{ ohm}^{-1}$ , an order of magnitude higher than that of  $\text{SmB}_6$  ( $0.02\text{ ohm}^{-1}$ ) (61) and  $\text{FeSi}$  ( $0.01\text{ ohm}^{-1}$ ) (62), and comparable to  $\text{Bi}_2\text{Se}_3$  (67). The unique combination of strong correlations, enhanced spin-orbit coupling, and high mobility in this 2D system makes the surface states of  $\text{U}_3\text{Bi}_4\text{Ni}_3$  particularly worthy of further investigation, as they could provide valuable insights into the complex interplay of these ingredients and potentially lead to the discovery of emergent quantum phenomena.

Our transport measurements and FEA analysis establish  $\text{U}_3\text{Bi}_4\text{Ni}_3$  as a Kondo insulator with a robust metallic surface state, one of the only known examples besides  $\text{SmB}_6$  and  $\text{YbB}_{12}$ . Notably, the surface state in  $\text{U}_3\text{Bi}_4\text{Ni}_3$  emerges at a much higher temperature, above the Kondo temperature, which calls for further investigation to understand the origin of this phenomenon. This distinction may provide new insights into the mechanism behind the surface states in Kondo insulators. Furthermore, the unique combination of high conductivity, mobility, and strong correlations observed in this system may give rise to emergent quantum phenomena, highlighting its significance for deepening our understanding of strongly correlated surface states in Kondo insulators.

#### IV. METHODS

**Sample Synthesis** Single crystals of  $\text{U}_3\text{Bi}_4\text{Ni}_3$  were prepared using the molten metal Flux method, with Bi as the solvent. Following the reported procedure (43), the raw elements were prepared

in molar ratios of U:Bi:Ni = 1:10:2 and placed into an Alumina crucible, which was sealed in a quartz tube with Argon gas at 0.265 atm. The furnace was heated to 1150 °C, and then cooled to a temperature of 650 °C at 5 °C/hr. To separate the crystals from the Bi Flux, the quartz tube was then taken out of the furnace at 650 °C and quickly inverted and placed into a centrifuge for 10 seconds. The  $U_3Bi_4Ni_3$  single crystals were confirmed with powder X-Ray diffraction (Cu- $K_\alpha$ ) with a Rigaku MiniFlex. Energy-dispersive X-ray spectroscopy measurements were performed using a Thermo Fisher Quattro environmental scanning electron microscope.

**Sample Preparation and Measurement** The samples prepared for resistivity measurements by polishing to a thickness of 100 – 200  $\mu\text{m}$  and Pt wire was attached using silver epoxy. A Hall bar is prepared with a standard four-wire measurement, through a pair of Hall contacts inserted between the voltage leads. The Corbino-disk geometry is prepared by drawing a ring of photo-resist on the sample face and around the sample edge, to prevent from shorting the top and bottoms surfaces. A gold sputter deposition of 50 nm forms an inner and outer electrode. This process is repeated on the bottom surface, to form another pair of electrodes. Electronic transport, specific heat, and magnetization measurements were performed in the Quantum Design Physical Property Measurement System using the Resistivity, specific heat and Vibrating Sample Magnetometer options.

**Finite Element Analysis** We studied the dependence of  $R_{12;12}$  and  $R_{12;34}$  on bulk to surface conductivity ratio by performing finite element analysis using COMSOL MULTIPHYSICS AC/DC module. We used Electric Currents and Electric Currents in Layered Shells interfaces of the AC/DC module to build the bulk and surface conducting channels, respectively. We used the same dimensions as the experimental samples in our simulation. In COMSOL, we can measure the value of  $R_{12;12}$  and  $R_{12;34}$  for a specific value of the bulk to surface conductivity ratio ( $\frac{\sigma_b t}{\sigma_s}$ ) used in simulation. By varying the bulk to surface conductivity ratios used in the simulation, we get two curves:  $R_{12;12}^s(\frac{\sigma_b t}{\sigma_s})$  and  $R_{12;34}^s(\frac{\sigma_b t}{\sigma_s})$ , where the superscript "s" represent simulation. On the other hand, we obtained  $R_{12;12}^e(T)$  and  $R_{12;34}^e(T)$  from experiment measurement, where the superscript "e" represent experiment. We fit the  $\frac{R_{12;12}^s(\frac{\sigma_b t}{\sigma_s})}{R_{12;34}^s(\frac{\sigma_b t}{\sigma_s})}$  from simulation and  $\frac{R_{12;12}^e(T)}{R_{12;34}^e(T)}$  from experiment to get  $\frac{\sigma_b t}{\sigma_s}(T)$ , which is shown in Fig 3(f) and (i). Because in simulation we know the value of  $\sigma_s$  used, we also have the curve of  $R_{12;12}^s \sigma_s(\frac{\sigma_b t}{\sigma_s})$ . Plugging in  $\frac{\sigma_b t}{\sigma_s}(T)$ , we get  $R_{12;12}^s \sigma_s(T)$ . Then assume  $R_{12;12}^s = R_{12;12}^e$  and plug in  $R_{12;12}^e(T)$ , we get  $\sigma_s(T)$ , which is shown in Fig 3.(e) and (h). In principle, we can also get  $\sigma_s(T)$  using  $R_{12;34}^s \sigma_s(\frac{\sigma_b t}{\sigma_s})$ . Both ways gave the same  $\sigma_s(T)$ , which we verified numerically. Plugging in  $\sigma_s(T)$  to  $\frac{\sigma_b t}{\sigma_s}(T)$ . we get  $\sigma_b(T)$ , which are shown in Fig 3. (d) and (g).

**Angle-Resolved Photoemission Spectroscopy Measurement** ARPES measurements were performed at beamline I05 of the Diamond Light Source (DLS). The angle resolution was  $\leq 0.2^\circ$  and the overall energy resolution was set  $\leq 25$  meV. The 98 eV and 92 eV photon energy were used to examine the difference between measurements performed on- and off-resonance at the uranium O edge. The fresh surfaces for ARPES measurement were obtained by cleaving the samples in situ in the measurement chamber. During the measurements, the chamber pressure was kept below  $2 \times 10^{-10}$  mbar, and the sample temperature was 6 K.

**Density Functional Theory** Electronic structures are calculated with the Density functional theory as implemented in the Vienna ab-initio Simulation Package (68), combining the PBE-type generalized gradient approximation (69) for the exchange-correlation interaction between electrons. The experimental crystal structure is employed. A cutoff energy for the plane-wave basis set is 350 eV. The k-mesh grid for the Brillouin zone is  $8 \times 8 \times 8$ . The Hubbard U correction for both the Ni d ( $U_d=0, 2, 4$  eV) and U f ( $U_f=0, 2, 4, 6$  eV) orbitals is employed. Spin-orbital coupling is included throughout. The wannier90 software (70) interface is employed to obtain the Wannier Hamiltonian for Wannier charge center calculations.

## ACKNOWLEDGMENTS

We acknowledge helpful discussions with Qimiao Si. **Funding:** Research at Washington University was supported by the National Science Foundation (NSF) Division of Materials Research Award DMR-2236528. CB acknowledges the NRT LinQ, supported by the NSF under Grant No. 2152221. Research at University of Michigan was supported by the Air Force Office of Scientific Research through the Multidisciplinary University Research Initiative, Award No. FA9550-23-1-0334 (XW and KS) and the Office of Naval Research through the Multidisciplinary University Research Initiative, Award No. N00014-20-1-2479 (WC and KS). BY acknowledges the financial support by the European Research Council (ERC Consolidator Grant “NonlinearTopo”, No. 815869) and the ISF - Personal Research Grant (No. 2932/21) and the DFG (CRC 183, A02). YLC acknowledges the support from the National Natural Science Foundation of China (No. U23A6002). We acknowledge Diamond Light Source for time on Beamline I05 under proposal number SI36513.

**Author contributions:** S.R., K.S. and B.Y. conceived and designed the study. C.B. synthesized the single crystalline samples of  $U_3Bi_4Ni_3$ . C.B. and H.S. performed the electrical transport and

magnetic measurements. G.X. fabricated devices using focused ion beam. X.W., W.C., W.L., Y.W. and K.S. performed the finite element analysis. D.W. and Y.C. performed the angle-resolved photoemission spectroscopy measurement. H.T. and B.Y. performed the Density Functional Theory calculations. S.L.G. performed the EDX measurements. Y.S.E, P.R., L.X., and R.C. performed the specific heat measurements. C.B. and S.R. wrote the manuscript with contributions from all authors. **Competing Interests:** The authors declare no competing interests. **Data and Materials Availability:** All data needed to evaluate the conclusions of this paper are present in the paper and the Supplemental Materials.

---

- [1] H. Tsunetsugu, M. Sigrist, and K. Ueda, The ground-state phase diagram of the one-dimensional Kondo lattice model, [Rev. Mod. Phys. 69, 809 \(1997\)](#).
- [2] R. Jullien, J. N. Fields, and S. Doniach, Zero-temperature real-space renormalization-group method for a Kondo-lattice model hamiltonian, [Phys. Rev. B 16, 4889 \(1977\)](#).
- [3] C. Lacroix and M. Cyrot, Phase diagram of the Kondo lattice, [Phys. Rev. B 20, 1969 \(1979\)](#).
- [4] N. Read, D. M. Newns, and S. Doniach, Stability of the Kondo lattice in the large- $n$  limit, [Phys. Rev. B 30, 3841 \(1984\)](#).
- [5] H. Kaga, H. Kubo, and T. Fujiwara, Coherent Kondo-lattice state and the crossover transitions in the anderson-lattice model, [Phys. Rev. B 37, 341 \(1988\)](#).
- [6] P. Kumar and N. S. Vidhyadhiraja, From mixed valence to the Kondo lattice regime, [Journal of Physics: Condensed Matter 23, 485601 \(2011\)](#).
- [7] W. A. Phelan, S. M. Koohpayeh, P. Cottingham, J. W. Freeland, J. C. Leiner, C. L. Broholm, and T. M. McQueen, Correlation between bulk thermodynamic measurements and the low-temperature-resistance plateau in  $\text{SmB}_6$ , [Phys. Rev. X 4, 031012 \(2014\)](#).
- [8] Y. Sato, Z. Xiang, Y. Kasahara, S. Kasahara, L. Chen, C. Tinsman, F. Iga, J. Singleton, N. L. Nair, N. Maksimovic, *et al.*, Topological surface conduction in Kondo insulator  $\text{YbB}_{12}$ , [Journal of Physics D: Applied Physics 54, 404002 \(2021\)](#).
- [9] L. Li, K. Sun, C. Kurdak, and J. Allen, Emergent mystery in the Kondo insulator samarium hexaboride, [Nature Reviews Physics 2, 463 \(2020\)](#).
- [10] J. C. Nickerson, R. M. White, K. N. Lee, R. Bachmann, T. H. Geballe, and G. W. Hull, Physical properties of

- smb<sub>6</sub>, [Phys. Rev. B \*\*3\*\*, 2030 \(1971\)](#).
- [11] P. S. Riseborough, Collapse of the coherence gap in Kondo semiconductors, [Phys. Rev. B \*\*68\*\*, 235213 \(2003\)](#).
- [12] I. Batko and M. Batkova, SmB<sub>6</sub>: Topological insulator or semiconductor with valence-fluctuation induced hopping transport?, [Solid state communications \*\*196\*\*, 18 \(2014\)](#).
- [13] T. Takimoto, SmB<sub>6</sub>: A promising candidate for a topological insulator, [Journal of the Physical Society of Japan \*\*80\*\*, 123710 \(2011\)](#).
- [14] F. Lu, J. Zhao, H. Weng, Z. Fang, and X. Dai, Correlated topological insulators with mixed valence, [Phys. Rev. Lett. \*\*110\*\*, 096401 \(2013\)](#).
- [15] J. Kim, K. Kim, C.-J. Kang, S. Kim, H. C. Choi, J.-S. Kang, J. D. Denlinger, and B. I. Min, Termination-dependent surface in-gap states in a potential mixed-valent topological insulator: SmB<sub>6</sub>, [Phys. Rev. B \*\*90\*\*, 075131 \(2014\)](#).
- [16] P. Thunström and K. Held, Topology of SmB<sub>6</sub> determined by dynamical mean field theory, [Phys. Rev. B \*\*104\*\*, 075131 \(2021\)](#).
- [17] L. Fu, Topological crystalline insulators, [Phys. Rev. Lett. \*\*106\*\*, 106802 \(2011\)](#).
- [18] H. Weng, J. Zhao, Z. Wang, Z. Fang, and X. Dai, Topological crystalline Kondo insulator in mixed valence ytterbium borides, [Phys. Rev. Lett. \*\*112\*\*, 016403 \(2014\)](#).
- [19] Z.-H. Zhu, A. Nicolaou, G. Levy, N. P. Butch, P. Syers, X. F. Wang, J. Paglione, G. A. Sawatzky, I. S. Elfimov, and A. Damascelli, Polarity-driven surface metallicity in smb<sub>6</sub>, [Phys. Rev. Lett. \*\*111\*\*, 216402 \(2013\)](#).
- [20] K. Hagiwara, Y. Ohtsubo, M. Matsunami, S.-i. Ideta, K. Tanaka, H. Miyazaki, J. E. Rault, P. L. Fèvre, F. Bertran, A. Taleb-Ibrahimi, R. Yukawa, M. Kobayashi, K. Horiba, H. Kumigashira, K. Sumida, T. Okuda, F. Iga, and S.-i. Kimura, Surface Kondo effect and non-trivial metallic state of the Kondo insulator YbB<sub>12</sub>, [Nature Communications \*\*7\*\*, 12690 \(2016\)](#).
- [21] V. B. Zabolotnyy, K. Fürsich, R. J. Green, P. Lutz, K. Treiber, C.-H. Min, A. V. Dukhnenko, N. Y. Shitsevalova, V. B. Filipov, B. Y. Kang, B. K. Cho, R. Sutarto, F. He, F. Reinert, D. S. Inosov, and V. Hinkov, Chemical and valence reconstruction at the surface of SmB<sub>6</sub> revealed by means of resonant soft x-ray reflectometry, [Phys. Rev. B \*\*97\*\*, 205416 \(2018\)](#).
- [22] P. Hlawenka, K. Siemensmeyer, E. Weschke, A. Varykhalov, J. Sánchez-Barriga, N. Y. Shitsevalova, A. Dukhnenko, V. Filipov, S. Gabáni, K. Flachbart, *et al.*, Samarium hexaboride is a trivial surface conductor, [Nature Communications \*\*9\*\*, 517 \(2018\)](#).

- [23] B. Tan, Y.-T. Hsu, B. Zeng, M. C. Hatnean, N. Harrison, Z. Zhu, M. Hartstein, M. Kiourlappou, A. Srivastava, M. Johannes, *et al.*, Unconventional fermi surface in an insulating state, [Science](#) **349**, 287 (2015).
- [24] M. Hartstein, W. Toews, Y.-T. Hsu, B. Zeng, X. Chen, M. C. Hatnean, Q. Zhang, S. Nakamura, A. Padgett, G. Rodway-Gant, *et al.*, Fermi surface in the absence of a fermi liquid in the Kondo insulator  $\text{SmB}_6$ , [Nature Physics](#) **14**, 166 (2018).
- [25] P. G. LaBarre, A. Rydh, J. Palmer-Fortune, J. Frothingham, S. Hannahs, A. P. Ramirez, and N. A. Fortune, Magnetoquantum oscillations in the specific heat of a topological Kondo insulator, [Journal of Physics: Condensed Matter](#) **34**, 36LT01 (2022).
- [26] Z. Xiang, Y. Kasahara, T. Asaba, B. Lawson, C. Tinsman, L. Chen, K. Sugimoto, S. Kawaguchi, Y. Sato, G. Li, *et al.*, Quantum oscillations of electrical resistivity in an insulator, [Science](#) **362**, 65 (2018).
- [27] Y. Sato, Z. Xiang, Y. Kasahara, T. Taniguchi, S. Kasahara, L. Chen, T. Asaba, C. Tinsman, H. Murayama, O. Tanaka, *et al.*, Unconventional thermal metallic state of charge-neutral fermions in an insulator, [Nature Physics](#) **15**, 954 (2019).
- [28] Z. Xiang, L. Chen, K.-W. Chen, C. Tinsman, Y. Sato, T. Asaba, H. Lu, Y. Kasahara, M. Jaime, F. Balakirev, *et al.*, Unusual high-field metal in a Kondo insulator, [Nature Physics](#) **17**, 788 (2021).
- [29] Z. Xiang, K.-W. Chen, L. Chen, T. Asaba, Y. Sato, N. Zhang, D. Zhang, Y. Kasahara, F. Iga, W. A. Coniglio, Y. Matsuda, J. Singleton, and L. Li, Hall anomaly, quantum oscillations and possible lifshitz transitions in Kondo insulator  $\text{YbB}_{12}$ : Evidence for unconventional charge transport, [Phys. Rev. X](#) **12**, 021050 (2022).
- [30] C. A. Mizzi, S. K. Kushwaha, P. F. Rosa, W. A. Phelan, D. C. Arellano, L. A. Pressley, T. M. McQueen, M. K. Chan, and N. Harrison, The reverse quantum limit and its implications for unconventional quantum oscillations in  $\text{YbB}_{12}$ , [Nature Communications](#) **15**, 1607 (2024).
- [31] D. Chowdhury, I. Sodemann, and T. Senthil, Mixed-valence insulators with neutral fermi surfaces, [Nature communications](#) **9**, 1766 (2018).
- [32] G. Baskaran, Majorana fermi sea in insulating  $\text{SmB}_6$ : A proposal and a theory of quantum oscillations in Kondo insulators, [arXiv](#) **1507**, 03477 (2015).
- [33] O. Erten, P.-Y. Chang, P. Coleman, and A. M. Tsvelik, Skyrme insulators: Insulators at the brink of superconductivity, [Phys. Rev. Lett.](#) **119**, 057603 (2017).
- [34] P. Coleman, E. Miranda, and A. Tsvelik, Are Kondo insulators gapless?, [Physica B: Condensed Matter](#) **186-188**, 362 (1993).
- [35] P. Coleman, E. Miranda, and A. Tsvelik, Odd-frequency pairing in the Kondo lattice, [Phys. Rev. B](#) **49**, 8955

(1994).

- [36] P. Coleman, L. B. Ioffe, and A. M. Tsvelik, Simple formulation of the two-channel Kondo model, [Phys. Rev. B \*\*52\*\*, 6611 \(1995\)](#).
- [37] T. Senthil, S. Sachdev, and M. Vojta, Fractionalized fermi liquids, [Phys. Rev. Lett. \*\*90\*\*, 216403 \(2003\)](#).
- [38] T. Yoshida, R. Peters, and N. Kawakami, Non-hermitian perspective of the band structure in heavy-fermion systems, [Phys. Rev. B \*\*98\*\*, 035141 \(2018\)](#).
- [39] Y. Nagai, Y. Qi, H. Isobe, V. Kozii, and L. Fu, DMFT reveals the non-hermitian topology and Fermi arcs in heavy-fermion systems, [Phys. Rev. Lett. \*\*125\*\*, 227204 \(2020\)](#).
- [40] J. Smith and E. Kmetko, Magnetism or bonding: A nearly periodic table of transition elements, [Journal of the Less Common Metals \*\*90\*\*, 83 \(1983\)](#).
- [41] T. Endstra, G. J. Nieuwenhuys, and J. A. Mydosh, Hybridization model for the magnetic-ordering behavior of uranium- and cerium-based 1:2:2 intermetallic compounds, [Phys. Rev. B \*\*48\*\*, 9595 \(1993\)](#).
- [42] Q. G. Sheng, B. R. Cooper, and S. P. Lim, First-principle study of hybridization effects and magnetic ordering in correlated-electron uranium systems, [Phys. Rev. B \*\*50\*\*, 9215 \(1994\)](#).
- [43] T. Klimczuk, H.-o. Lee, F. Ronning, T. Durakiewicz, N. Kurita, H. Volz, E. D. Bauer, T. McQueen, R. Movshovich, R. J. Cava, and J. D. Thompson, Physical properties of the uranium ternary compounds  $U_3Bi_4M_3$  ( $M = Ni, Rh$ ), [Phys. Rev. B \*\*77\*\*, 245111 \(2008\)](#).
- [44] S.-H. Baek, N. J. Curro, T. Klimczuk, H. Sakai, E. D. Bauer, F. Ronning, and J. D. Thompson, Hybridization-driven gap in  $U_3Bi_4Ni_3$ : A  $^{209}Bi$  NMR/NQR study, [Phys. Rev. B \*\*79\*\*, 195120 \(2009\)](#).
- [45] B. Gorshunov, N. Sluchanko, A. Volkov, M. Dressel, G. Knebel, A. Loidl, and S. Kunii, Low-energy electro-dynamics of  $SmB_6$ , [Phys. Rev. B \*\*59\*\*, 1808 \(1999\)](#).
- [46] J. Yamaguchi, A. Sekiyama, M. Kimura, H. Sugiyama, Y. Tomida, G. Funabashi, S. Komori, T. Balashov, W. Wulfhekkel, T. Ito, *et al.*, Different evolution of the intrinsic gap in strongly correlated  $SmB_6$  in contrast to  $YbB_{12}$ , [New Journal of Physics \*\*15\*\*, 043042 \(2013\)](#).
- [47] X. Zhang, N. P. Butch, P. Syers, S. Ziemak, R. L. Greene, and J. Paglione, Hybridization, inter-ion correlation, and surface states in the Kondo insulator  $SmB_6$ , [Phys. Rev. X \*\*3\*\*, 011011 \(2013\)](#).
- [48] W. Ruan, C. Ye, M. Guo, F. Chen, X. Chen, G.-M. Zhang, and Y. Wang, Emergence of a coherent in-gap state in the  $SmB_6$  Kondo insulator revealed by scanning tunneling spectroscopy, [Phys. Rev. Lett. \*\*112\*\*, 136401 \(2014\)](#).
- [49] Y. Takeda, M. Arita, M. Higashiguchi, K. Shimada, H. Namatame, M. Taniguchi, F. Iga, and T. Takabatake,

- High-resolution photoemission study of the temperature-dependent  $c-f$  hybridization gap in the Kondo semiconductor  $\text{YbB}_{12}$ , [Phys. Rev. B \*\*73\*\*, 033202 \(2006\)](#).
- [50] N. Nagaosa, J. Sinova, S. Onoda, A. H. MacDonald, and N. P. Ong, Anomalous Hall effect, [Rev. Mod. Phys. \*\*82\*\*, 1539 \(2010\)](#).
- [51] N. W. Ashcroft and N. D. Mermin, *Solid state physics* (Cengage Learning, 2022).
- [52] P. M. Levy, Extraordinary Hall effect in Kondo-type systems: Contributions from anomalous velocity, [Phys. Rev. B \*\*38\*\*, 6779 \(1988\)](#).
- [53] A. Fert, A. Friederich, and A. Hamzic, Hall effect in dilute magnetic alloys, [Journal of Magnetism and Magnetic Materials \*\*24\*\*, 231 \(1981\)](#).
- [54] J. Kondo, Effect of ordinary scattering on exchange scattering from magnetic impurity in metals, [Phys. Rev. \*\*169\*\*, 437 \(1968\)](#).
- [55] K. Nagaoka, T. Jamneala, M. Grobis, and M. F. Crommie, Temperature dependence of a single Kondo impurity, [Phys. Rev. Lett. \*\*88\*\*, 077205 \(2002\)](#).
- [56] Q. Y. Chen, X. B. Luo, D. H. Xie, M. L. Li, X. Y. Ji, R. Zhou, Y. B. Huang, W. Zhang, W. Feng, Y. Zhang, L. Huang, Q. Q. Hao, Q. Liu, X. G. Zhu, Y. Liu, P. Zhang, X. C. Lai, Q. Si, and S. Y. Tan, Orbital-selective Kondo entanglement and antiferromagnetic order in  $\text{USb}_2$ , [PRL \*\*123\*\*, 106402 \(2019\)](#).
- [57] H. Siddiquee, C. Broyles, E. Kotta, S. Liu, S. Peng, T. Kong, B. Kang, Q. Zhu, Y. Lee, L. Ke, H. Weng, J. D. Denlinger, L. A. Wray, and S. Ran, Breakdown of the scaling relation of anomalous Hall effect in Kondo lattice ferromagnet  $\text{USbTe}$ , [Nature Communications \*\*14\*\*, 527 \(2023\)](#).
- [58] M. Neupane, N. Alidoust, S. Xu, T. Kondo, Y. Ishida, D.-J. Kim, C. Liu, I. Belopolski, Y. Jo, T.-R. Chang, *et al.*, Surface electronic structure of the topological Kondo-insulator candidate correlated electron system  $\text{SmB}_6$ , [Nature communications \*\*4\*\*, 2991 \(2013\)](#).
- [59] J. Jiang, S. Li, T. Zhang, Z. Sun, F. Chen, Z. Ye, M. Xu, Q. Ge, S. Tan, X. Niu, *et al.*, Observation of possible topological in-gap surface states in the Kondo insulator  $\text{SmB}_6$  by photoemission, [Nature communications \*\*4\*\*, 3010 \(2013\)](#).
- [60] Y. S. Eo, K. Sun, i. m. c. Kurdak, D.-J. Kim, and Z. Fisk, Inverted resistance measurements as a method for characterizing the bulk and surface conductivities of three-dimensional topological insulators, [Phys. Rev. Appl. \*\*9\*\*, 044006 \(2018\)](#).
- [61] Y. S. Eo, A. Rakoski, J. Lucien, D. Mihalirov, Ç. Kurdak, P. F. Rosa, and Z. Fisk, Transport gap in  $\text{SmB}_6$  protected against disorder, [Proceedings of the National Academy of Sciences \*\*116\*\*, 12638 \(2019\)](#).

- [62] Y. S. Eo, K. Avers, J. A. Horn, H. Yoon, S. R. Saha, A. Suarez, M. S. Fuhrer, and J. Paglione, Extraordinary bulk-insulating behavior in the strongly correlated materials FeSi and FeSb<sub>2</sub>, [Applied Physics Letters](#) **122**, 233102 (2023).
- [63] M. Dzero, K. Sun, V. Galitski, and P. Coleman, Topological kondo insulators, [PRL](#) **104**, 106408 (2010).
- [64] D.-J. Kim, J. Xia, and Z. Fisk, Topological surface state in the Kondo insulator samarium hexaboride, [Nature materials](#) **13**, 466 (2014).
- [65] J. Yong, Y. Jiang, D. Usanmaz, S. Curtarolo, X. Zhang, L. Li, X. Pan, J. Shin, I. Takeuchi, and R. L. Greene, Robust topological surface state in Kondo insulator SmB<sub>6</sub> thin films, [Applied Physics Letters](#) **105**, 222403 (2014).
- [66] T. Susaki, A. Sekiyama, K. Kobayashi, T. Mizokawa, A. Fujimori, M. Tsunekawa, T. Muro, T. Matsushita, S. Suga, H. Ishii, T. Hanyu, A. Kimura, H. Namatame, M. Taniguchi, T. Miyahara, F. Iga, M. Kasaya, and H. Harima, Low-energy electronic structure of the Kondo insulator YbB<sub>12</sub>, [Phys. Rev. Lett.](#) **77**, 4269 (1996).
- [67] Y. S. Kim, M. Brahlek, N. Bansal, E. Edrey, G. A. Kapilevich, K. Iida, M. Tanimura, Y. Horibe, S.-W. Cheong, and S. Oh, Thickness-dependent bulk properties and weak antilocalization effect in topological insulator Bi<sub>2</sub>Se<sub>3</sub>, [Phys. Rev. B](#) **84**, 073109 (2011).
- [68] G. Kresse and J. Furthmüller, Efficient iterative schemes for ab initio total-energy calculations using a plane-wave basis set, [Phys. Rev. B](#) **54**, 11169 (1996).
- [69] J. P. Perdew, K. Burke, and M. Ernzerhof, Generalized gradient approximation made simple, [Phys. Rev. Lett.](#) **77**, 3865 (1996).
- [70] G. Pizzi, V. Vitale, R. Arita, S. Blügel, F. Freimuth, G. Géranton, M. Gibertini, D. Gresch, C. Johnson, T. Koretsune, *et al.*, Wannier90 as a community code: new features and applications, [Journal of Physics: Condensed Matter](#) **32**, 165902 (2020).

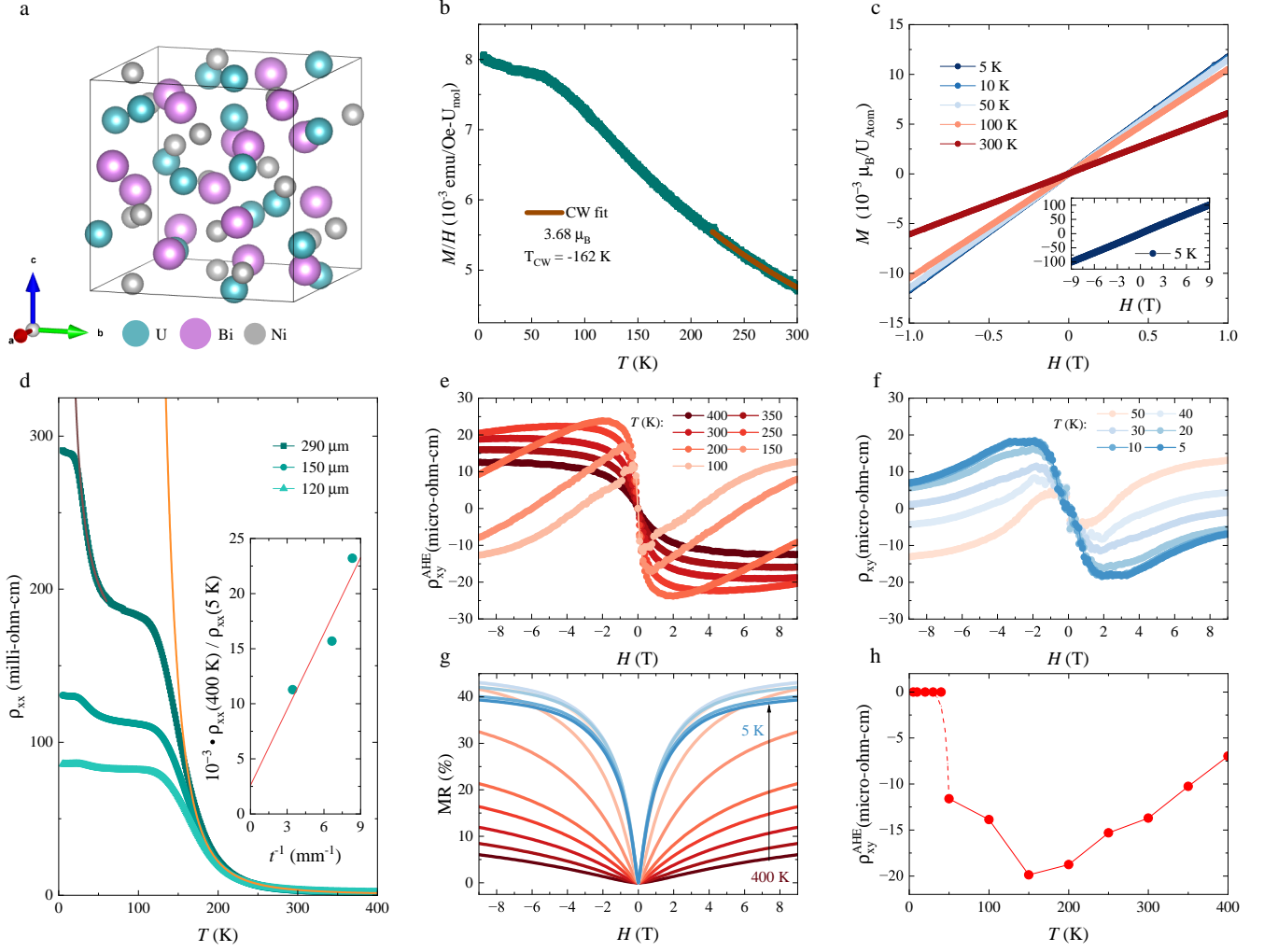


**Fig. 1. Bulk Kondo Insulator Characterization** (a) The crystal structure of  $U_3Bi_4Ni_3$ , space group No. 220 (I-43d). (b) The magnetic susceptibility measured from room temperature down to 5 K, with a magnetic field of 0.1 T. (c) Magnetic field sweeps up to 1 T for various temperatures between 5 and 300 K. The inset displays a 9 T field sweep at 5 K. (d) The temperature dependence of  $\rho_{xx}$ , measured on a single crystal which was successively polished to thicknesses of 290, 150, and 120  $\mu m$ , with a fitting applied above 200 K (orange,  $\Delta=95$  meV) and between 30 and 60 K (brown,  $\Delta=1.5$  meV). The inset displays  $\rho(400 K)/\rho(5 K)$  vs  $t^{-1}$ , modeled by the equation  $\rho(400 K)/\rho = (2 \sigma_s/\sigma_{400 K}) t^{-1} + \sigma_b/\sigma_{400 K}$ . The linear fitting provides a slope of  $2.3 \pm 0.8$  and an intercept of  $3 \pm 5 \times 10^{-3}$ . (e, f) The Hall resistivity ( $\rho_{xy}$ ) field sweeps for  $T \geq 100$  K are displayed in (e), while those for  $T \leq 50$  K are shown in (f). (g) The magneto-resistance measured up to 9 T and presented for a variety of temperatures between 400 K and 5 K. (h) The anomalous Hall resistivity ( $\rho_{xy}^{AHE}$ ), extracted from the two-band + C fittings (see SI).

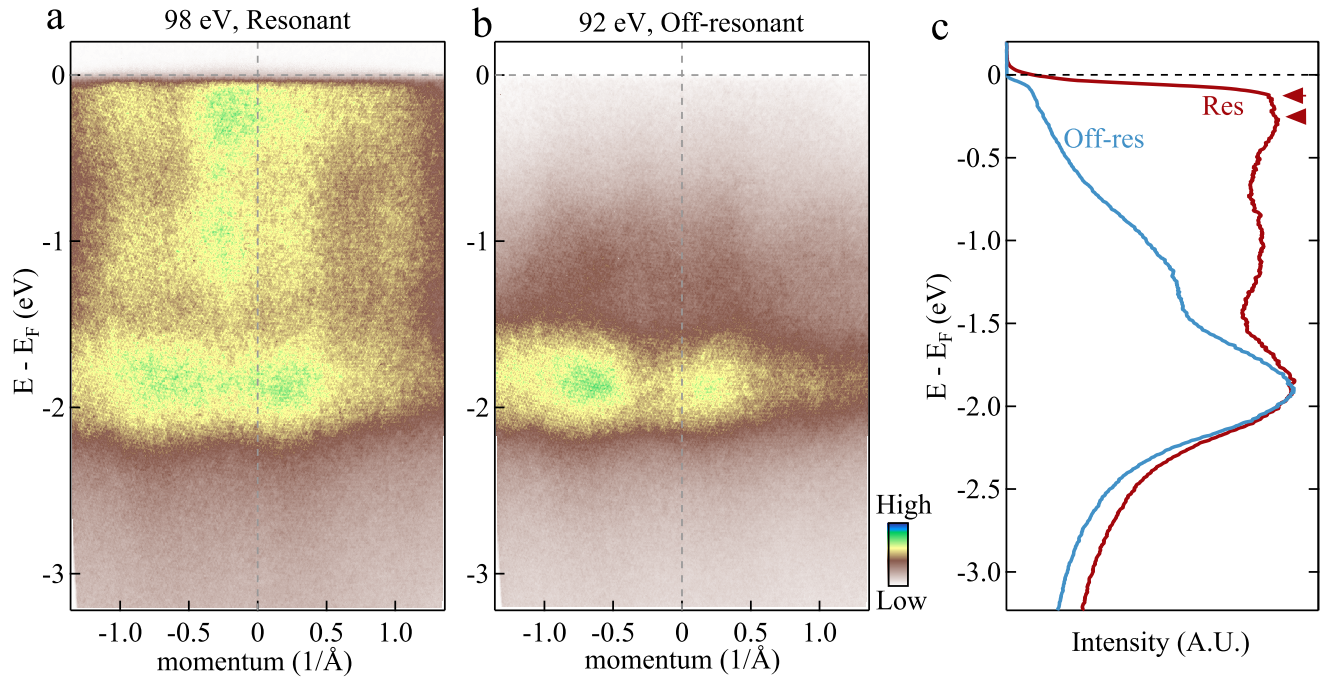


**Fig. 2. Resonant Enhanced ARPES** (a) The intensity map of Energy versus Angle for the resonant condition of 98 eV. (b) The off-resonant condition, with a photon energy of 92 eV. (c) The integrated energy distribution curve (EDC) of the resonant and off-resonant conditions, demonstrating *f*-band weight near  $E_F$ . All data were taken at 20 K.

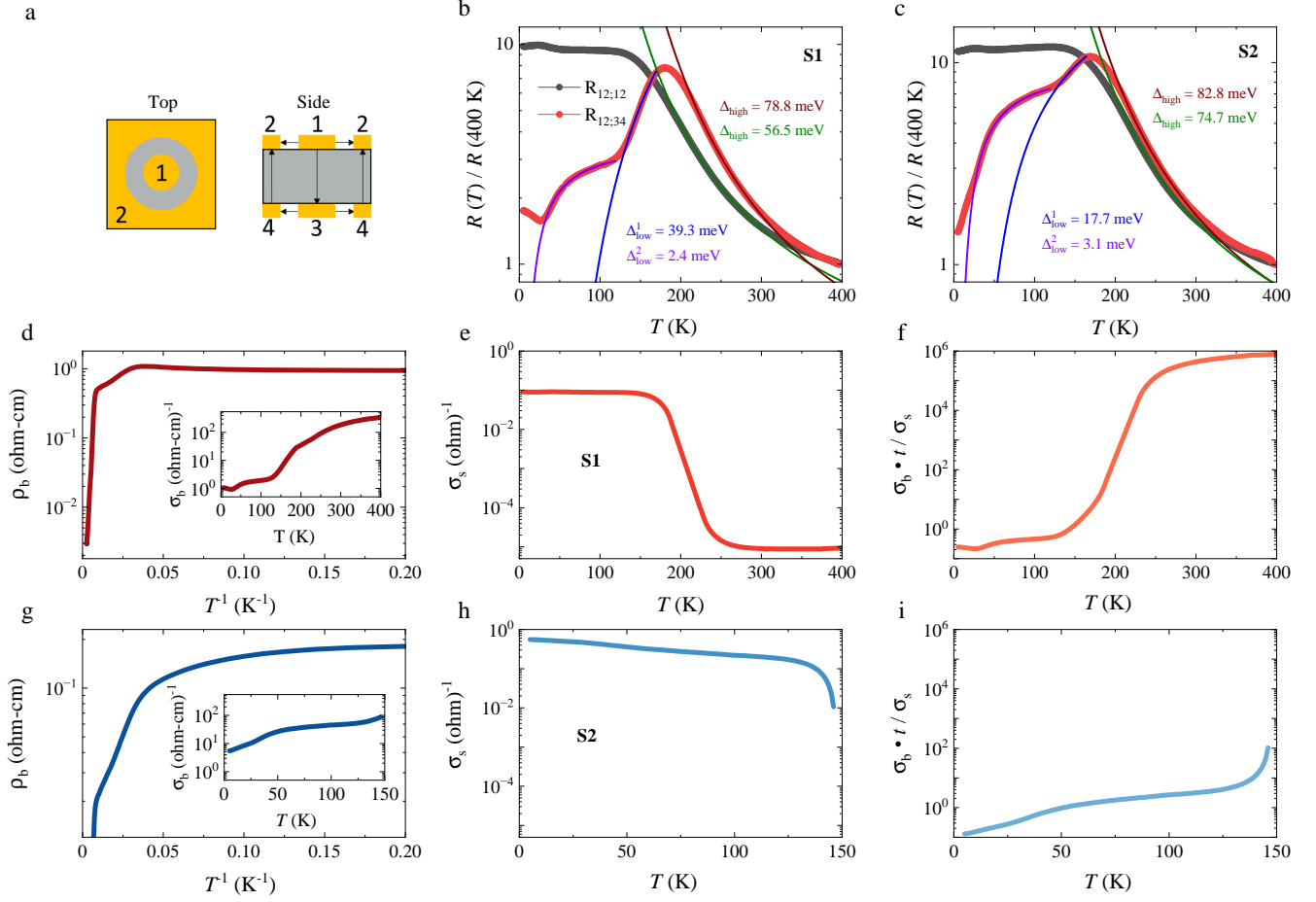


**Fig. 3. Corbino-disk and Finite Element Analysis** (a) The measurement geometry of the Corbino-disk, shown from the top and cross-sectional side view. (b, c) Corbino-disk samples 1 and 2 measured in the  $R_{12;12}$  and  $R_{12;34}$  configurations. (d, e) Using finite element analysis (FEA) to simulate the transport of sample 1, the bulk resistivity is plotted in (d), with the bulk conductivity in the inset, and the surface conductivity is displayed in (e). (f) The ratio of the bulk and surface conductivity, with  $t = 210\ \mu\text{m}$ . (g-i) The FEA results for sample 2, with a thickness of  $130\ \mu\text{m}$ , presented below the surface state onset.

# SI : High temperature surface state in Kondo insulator $U_3Bi_4Ni_3$

arXiv:2502.03448v1 [cond-mat.str-el] 5 Feb 2025

## I. SAMPLE VARIATION

The two samples used for the Corbino disk measurements show similar qualitative behavior, but quantitatively, there is a difference in their bulk and surface conductivities. This variation is likely due to impurity band or in-gap states, possibly originating from embedded flux during sample synthesis. To investigate this, we performed Energy-dispersive X-ray spectroscopy (EDX) measurements to characterize the chemical composition and also carried out specific heat measurements.

As summarized in Table S1, samples 1 and 2 exhibit small variations in their chemical composition, with approximately 2% differences in U and Ni content, while the Bi content remains nearly identical. We also measured three additional samples, which showed similar trends in their chemical composition variations. These slight differences in chemical composition could potentially explain the observed variations in bulk and surface conductivity.

We also measured the specific heat of samples S1 and S2 (see Fig. S1), both of which display very similar behavior, comparable to the data reported in a previous study (43). The absence of a noticeable electronic contribution to the specific heat confirms the insulating nature of the bulk material. Although impurities may introduce a minor electronic contribution, it remains minimal compared to the bulk response.

## II. LOW TEMPERATURE CHARACTERIZATION

The presence of magnetic order at low temperatures was investigated using AC magnetization in our dilution refrigerator. We did not detect any presence of a magnetic transition down to 35 mK (see Fig. S2), consistent with previous specific heat data taken down to 500 mK (43).

## III. MAGNETO-TRANSPORT FITTINGS

The transverse and longitudinal resistivity was measured in single crystals of  $\text{U}_3\text{Bi}_4\text{Ni}_3$  using magnetic fields up to 9 T. The symmetric component of the change in the longitudinal signal ( $\Delta\rho_{xx}$ ) and the asymmetric component of the transverse voltage ( $\rho_{xy}$ ) are used in the fittings. The two band (51) +  $C$  fittings are performed in Origin Lab, using a simultaneous fitting of  $\Delta\rho_{xx}(H)$  in the range of  $-9 \text{ T} \leq H \leq 9 \text{ T}$  and  $\rho_{xy}(H)$  in a range above polarization field dependence ( $2 \text{ T} \leq H \leq 9 \text{ T}$ ). A fit that shared both mobility and number density could not converge, so the number density was

fitted independently while the mobility was shared. Once the fitting for a field sweep was converged, the constant offset from the two-band model is taken to be  $\rho_{xy}^{\text{AHE}}$ .

The sample fittings for the 300 K and 5 K field sweeps are shown in Fig. S3. The 300 K fitting shows good agreement in the selected range and is extended to the full field range for clarity. The simultaneous fitting with  $\Delta\rho_{xx}$  is shown in Fig. S3b. The low temperature fitting for the Hall signal shows excellent agreement with the conventional two-band field dependence in Fig. S3c, and the longitudinal component also has a qualitatively good fit. The longitudinal component has a mismatch with the fitting endpoints. This is due to the MR not completely saturating at high fields, despite being the expectation from the Drude description (51).

The results of the fittings are shown in Fig. S4. In the high-temperature regime, the electronic transport is dominated by the hole-type carriers. The hole number density,  $\eta_h$ , is at a maximum around 300 K and the activated carrier are removed as the temperature decreases. This trend continues until a crossover in the carrier at 150-200 K, which aligns with the onset of the surface state in the Corbino disk measurements. Below this temperature,  $\eta_e$  overtakes  $\eta_h$  by nearly 4 orders of magnitude. A similar phenomenon is seen in the mobility parameters, where  $\mu_h$  surpasses  $\mu_e$  by 5 orders of magnitude. Below 50 K, there is a signature of the hole-like band hybridizing with the the  $f$ -orbital moments, resulting in an enhanced number density with suppressed mobility. The temperature dependence can be understood through the energy scale of the surface state, shifting the chemical potential, and Kondo interaction renormalizing the band gap.

#### IV. FIRST PRINCIPLES CALCULATIONS

Results for DFT+U calculations are shown in Fig. S5. The calculations predict a metallic band structure when Hubbard  $U$  correction is not applied. The  $U$   $f$  orbitals notably contribute to the bands near the charge neutral point, while the Ni  $d$  and Bi  $p$  orbitals are fully occupied and form the deeper valence bands. This metallic state clearly contradict the experimental results. Consequently, we applied Hubbard  $U$  corrections to both  $U$   $f$  and Ni  $d$  orbitals. The Hubbard  $U$  correction to the Ni  $d$  orbitals has minimal impact on the band structure, because these orbitals are completely filled. Upon applying Hubbard  $U$  to the uranium  $f$  electrons, the  $U$   $f$  bands at the Fermi energy become split, creating a global band gap. While at moderate Hubbard  $U$  value,  $U = 2$  eV, both conduction and valence bands are still dominated by  $f$  bands, for  $U = 4$  and 6 eV, the  $f$  bands are located far

away from the Fermi level, and the gap forms between the dispersive Ni  $d$  and Bi  $p$  bands, not the U  $f$  bands. This contradicts the behavior expected of  $U_3Bi_4Ni_3$  as a Kondo insulator, where  $f$  bands are supposed to contribute to the band gap, as supported by our transport and ARPES data. Furthermore, the predicted band gap is considerably larger than the observed value. These results reflect the limitations in dealing with the Kondo lattice system that is generic to DFT+ $U$  calculations, which consider the correlation effect as a local onsite interaction. In Kondo systems, the key interaction is between the localized  $f$  electrons and the conduction electrons, which involves dynamic screening and hybridization processes that DFT+ $U$  does not capture effectively. To better understand the electronic structure of  $U_3Bi_4Ni_3$ , we will need more advanced methods like DMFT.

Nevertheless, we analyzed the topology of the insulating state. As an example, we extracted the Wannier Hamiltonian from the band structure obtained with a Hubbard correction of 4 eV for the U- $f$  orbitals and 2 eV for the Ni- $d$  orbitals to examine its topology. The calculated Wannier charge centers ( $\theta$ ) on the six high-symmetry planes are shown in Fig. S6, revealing a trivial band topology in the Wilson loop. Again, since the orbital contributions are not fully captured by the DFT calculations, this topology analysis may not be reliable. More sophisticated methods, such as the Gutzwiller approach or DMFT, are necessary for more accurate studies in the future.

## V. INVERTED RESISTANCE DERIVATION

The inverted resistance is a non-local transport measurement, which supplies the current on the top of a sample and measures the voltage on the bottom. While some of current travels through the bulk of the sample, a majority of the transport will occur through surface channels when  $\rho_b \gg \rho_s$  (Fig. S7). The resistance measurement for  $R_{12;34}$  is performed by supplying current between pads (1) and (2) and measuring the voltage between pads (3) and (4). The measured voltage ( $V_{34}$ ) can be modeled by Ohm's law.

$$V_{34} = R_{bottom}^s * I_{bottom} \quad (1)$$

To understand how the measured voltage relates to the surface and bulk resistances, we first need to find out how much current travels on the bottom of the sample. This is accomplished by using the conservation of current (Eqn. 2) and Kirchhoff's voltage law (Eqn. 3).

$$I_{total} = I_{top} + I_{bottom} \quad (2)$$

$$I_{top} = I_{bottom} * \frac{R_{middle}^b + R_{bottom}^s + R_{side}^s}{R_{top}^s} \quad (3)$$

$$I_{bottom} = I_{total} * \frac{R_{top}^s}{R_{middle}^b + R_{top}^s + R_{bottom}^s + R_{side}^s} \quad (4)$$

Now that we know how much current is traveling on the bottom surface, in terms of the total current, we can substitute back into Eqn. 1.

$$V_{34} = I_{total} * \frac{R_{bottom}^s * R_{top}^s}{R_{middle}^b + R_{top}^s + R_{bottom}^s + R_{side}^s} \quad (5)$$

$$R_{12;34} = \frac{R_{bottom}^s * R_{top}^s}{R_{middle}^b + R_{top}^s + R_{bottom}^s + R_{side}^s} \quad (6)$$

We can simplify  $R_{12;34}$  in the limit that  $R_{middle}^b \gg R_{top}^s, R_{bottom}^s, R_{side}^s$ . This gives us a singular surviving term which consists of both the surface and bulk resistances.

$$R_{12;34} = \frac{R_{bottom}^s * R_{top}^s}{R_{middle}^b} \quad (7)$$

To convert to  $R_{12;34}$  in terms of  $\rho_b$  and  $\rho_s$ , we can use constant factors to capture the geometry of the sample and contact pads. We will assume  $R_{middle}^b$  will depend on the the geometry of the center pads and the sample thickness (ie.  $R_{middle}^b = C_{middle}^b * \rho_b / t$ ) and the surface resistances will depend on the surface resistivity and the geometry of the contact pads (ie.  $R_{top}^s = C_{top}^s * \rho_s$ ). We can absorb all these prefactors into  $C = C_{top}^s * C_{bottom}^s / C_{middle}^b$ .

$$R_{12;34} = C t \frac{\rho_s^2}{\rho_b} \propto \text{Exp}\left[-\frac{\Delta}{k_B T}\right] \quad (8)$$

**Table S1. SEM-EDX Compositional Analysis.**

Sample	U (%)	Bi (%)	Ni (%)
1	28.26±0.45	39.16±0.52	32.58±0.21
2	28.88±0.13	39.23±0.21	31.89±0.65
3	28.23±0.35	39.31±0.61	32.45±0.58
4	28.68±0.00	39.05±0.13	32.27±0.13
5	28.58±0.63	38.43±0.51	33.98±0.70

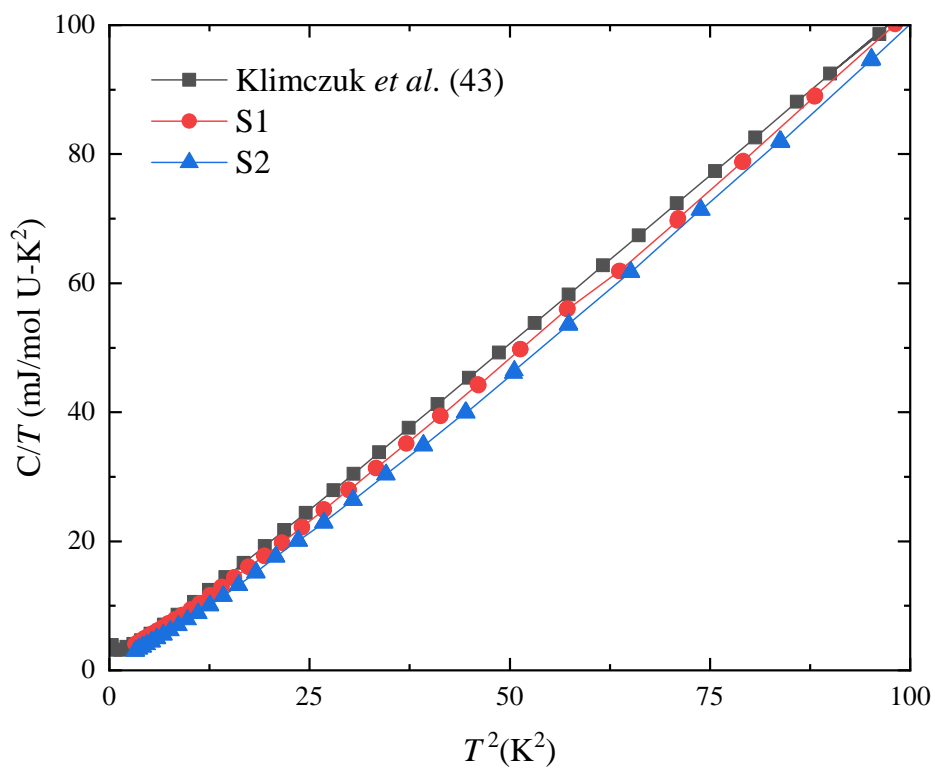


**Fig. S1. Thermodynamic Characterization.** Specific heat for two samples of  $U_3Bi_4Ni_3$ . No clear sample variation is observed.

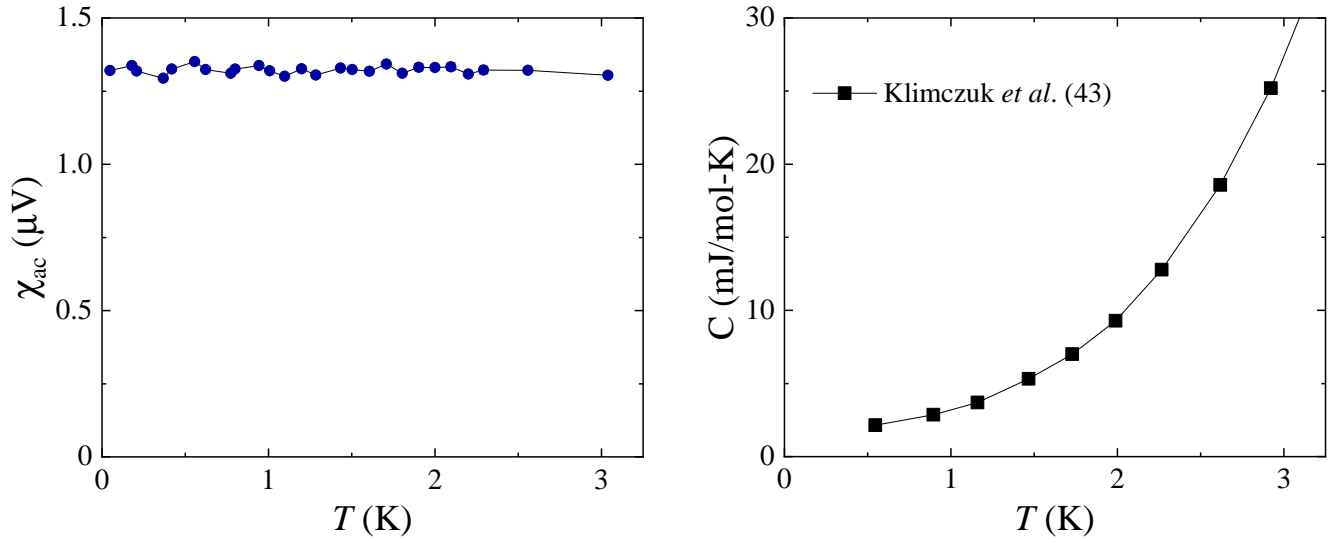


**Fig. S2. Low Temperature Characterization.** AC magnetometer measurements of  $\text{U}_3\text{Bi}_4\text{Ni}_3$  down to 35 mK, and specific heat measurements down to 500 mK from Klimczuk *et al.*(43).

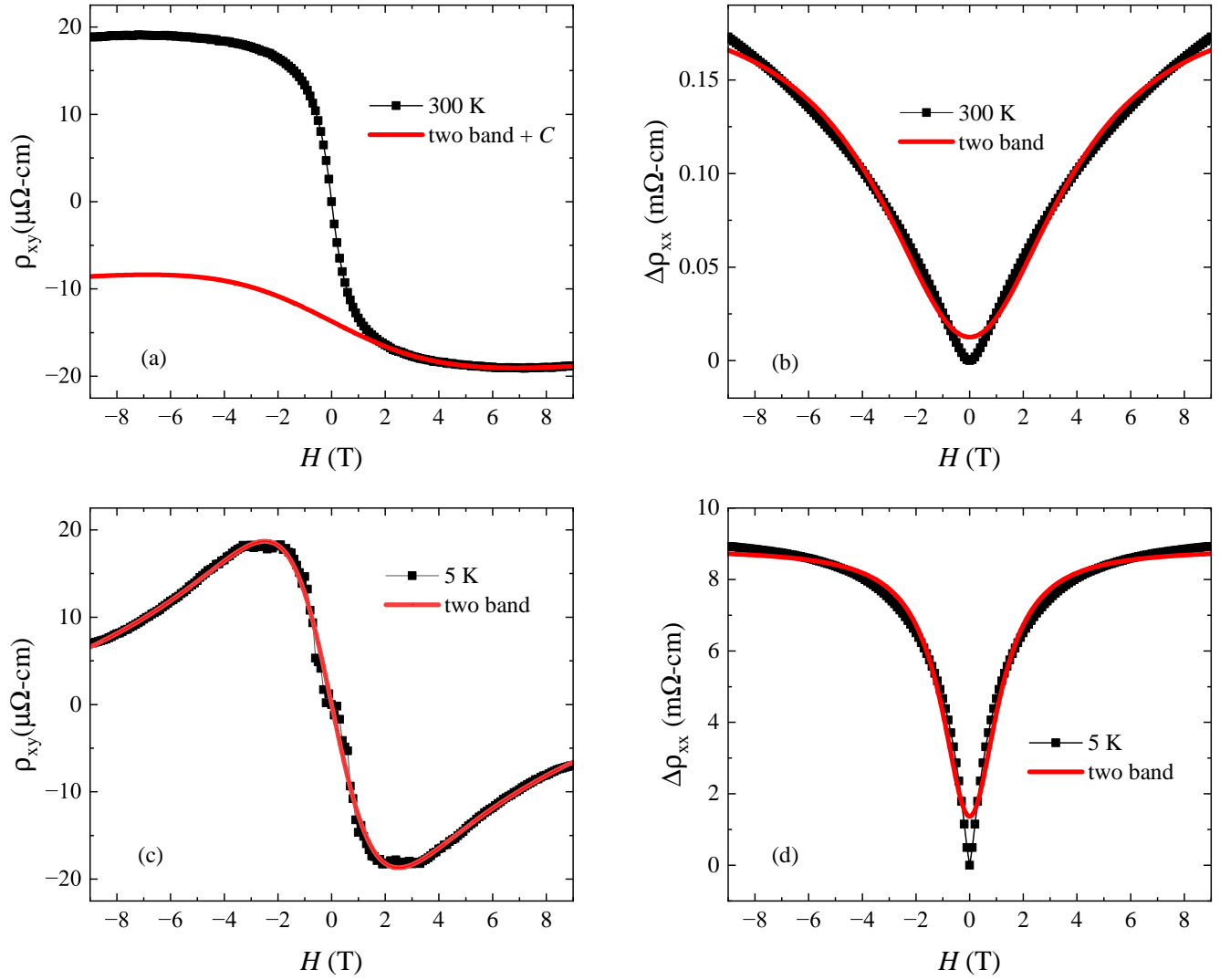


**Fig. S3. Two Band Magneto-Transport Fittings.** (a) Sample fitting for the 300 K field sweep for the asymmetric transverse resistivity,  $\rho_{xy}$ . (b) The change in longitudinal resistance,  $\Delta\rho_{xx}$ , fit with the conventional two band model. (c,d) Sample fitting for 5 K measurement, with fitting using the whole data range and  $C$  set to zero.

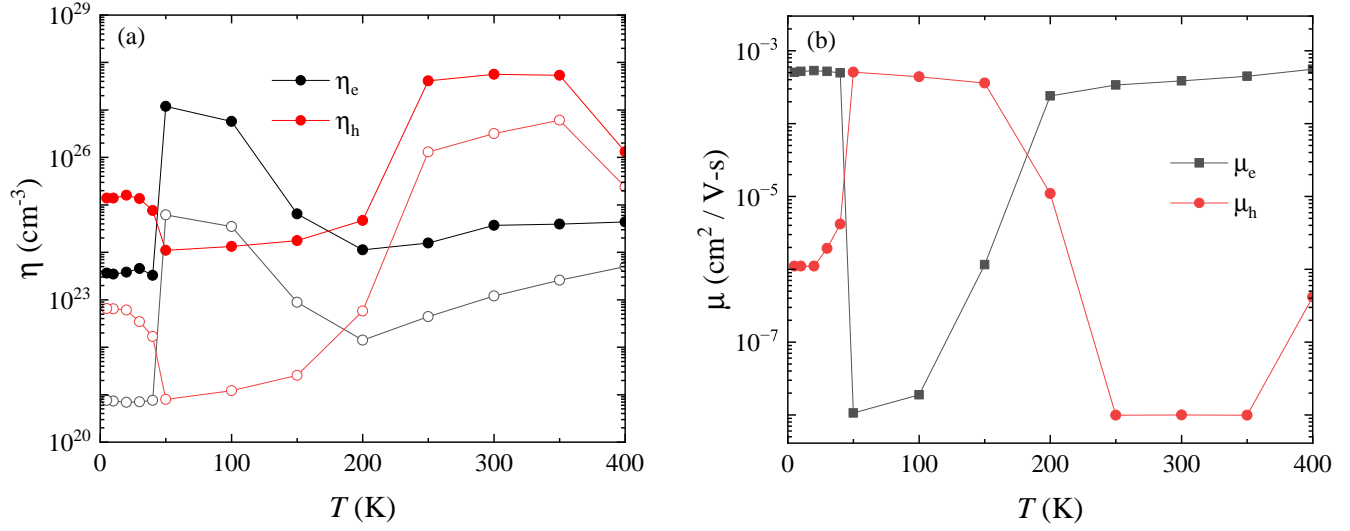


**Fig. S4. Two Band Magneto-Transport Fitting Parameters.** (a) The number density from the two band fitting parameters, which was fit independently for  $\rho_{xy}^{\text{assym}}$  (solid circles) and  $\Delta\rho_{xx}$  (open circles). (b) The mobility parameters for electron and hole carriers, which was the shared parameter in the fittings.

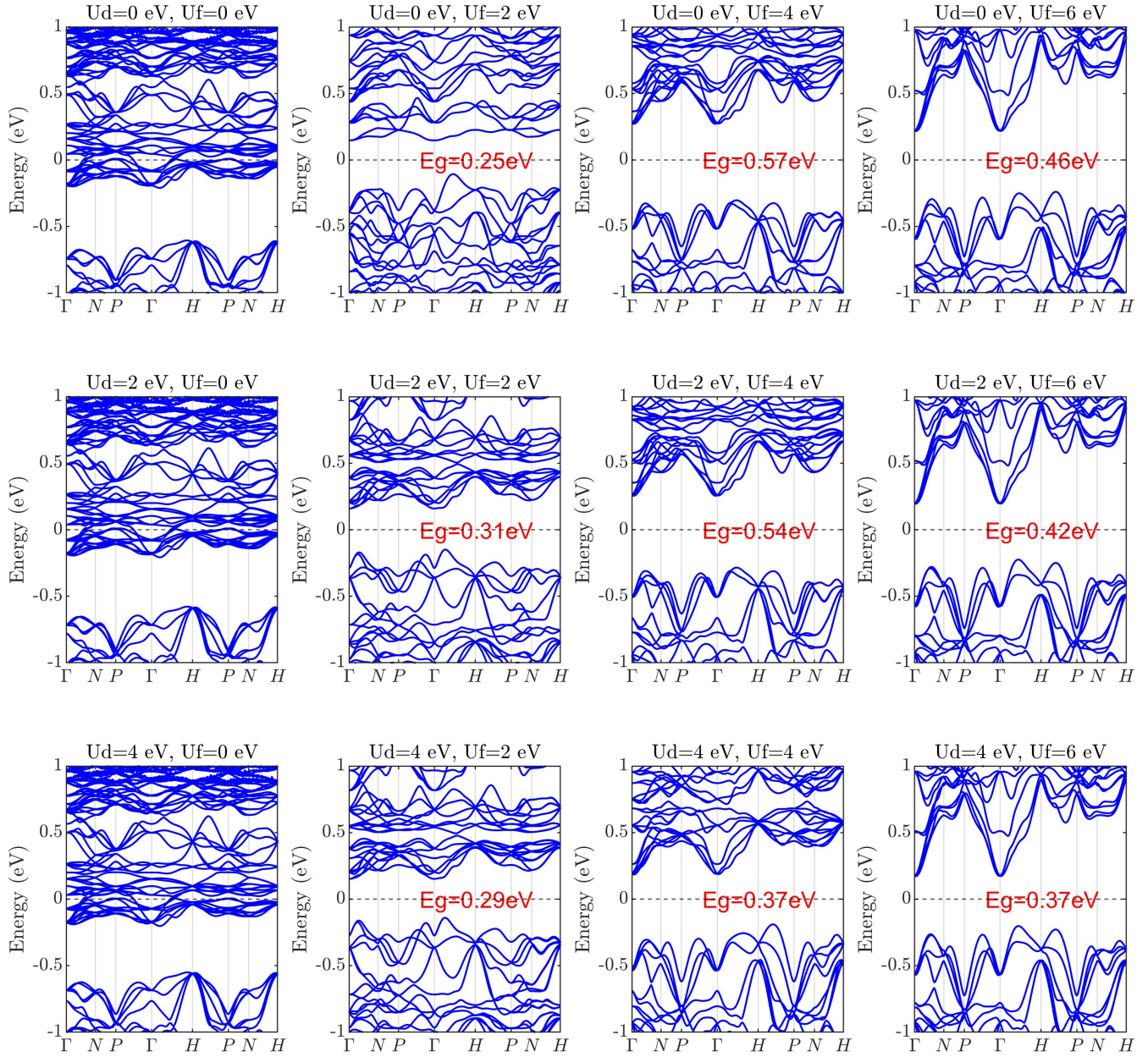


**Fig. S5. Electronic Structure.** Density Functional Theory (DFT) calculations, for a multitude of Hubbard  $U$  values applied to the Ni- $d$  and U- $f$  bands.

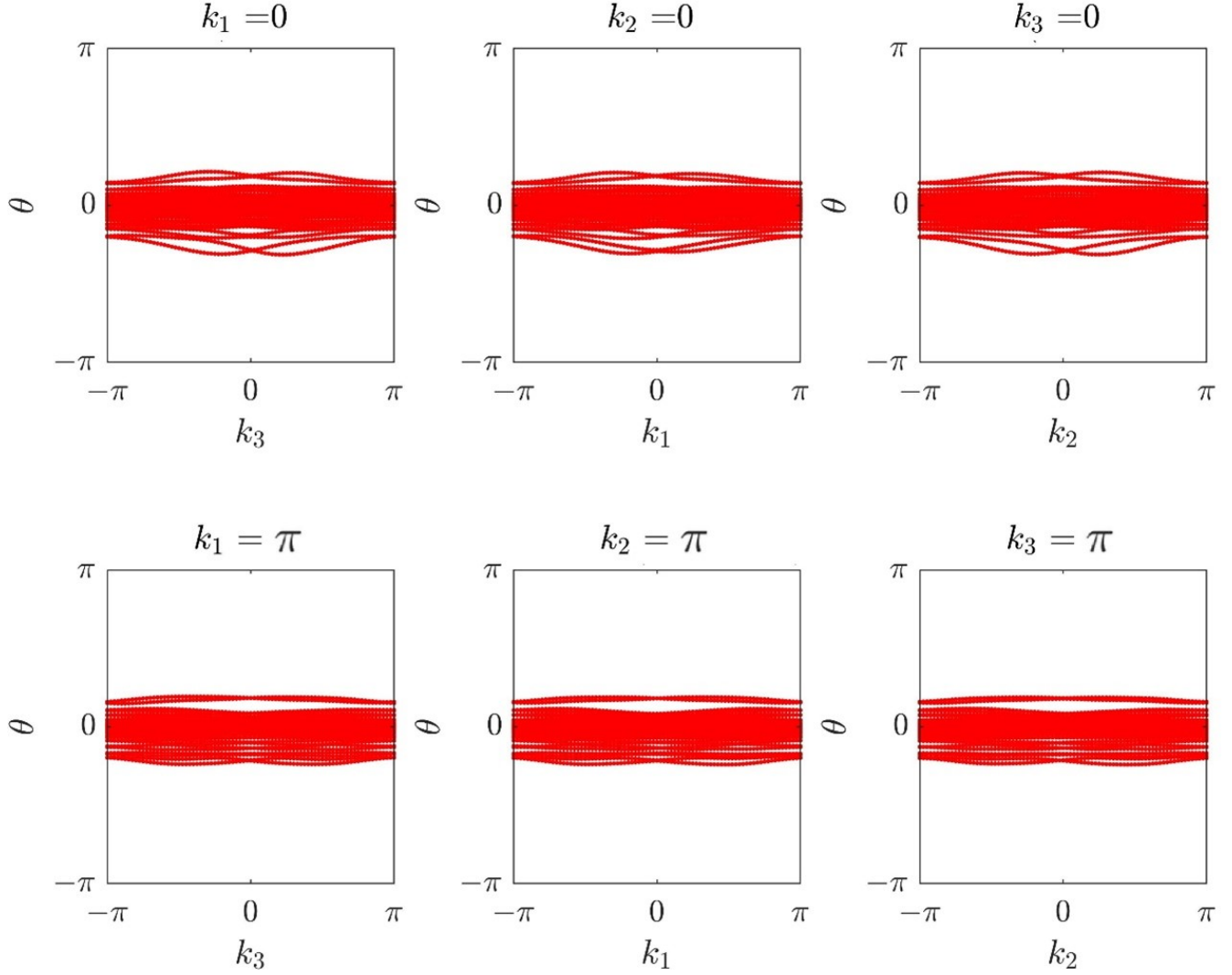


**Fig. S6. Topological Analysis of Electronic Structure.** Wilson loop calculations by the Wannier charge center ( $\theta$ ) evolution of  $U_3Bi_4Ni_3$  with Hubbard  $U$  correction 4 eV for  $U-f$  and 2 eV for  $Ni-d$ . The  $k_i$  ( $i=1,2,3$ ) indicates three reciprocal directions.  $k_i = 0$  ( $\pi$ ) in the title represents the 0 ( $\pi$ ) plane along that direction. Wilson loops indicate a topological trivial insulator in the DFT+ $U$  level.

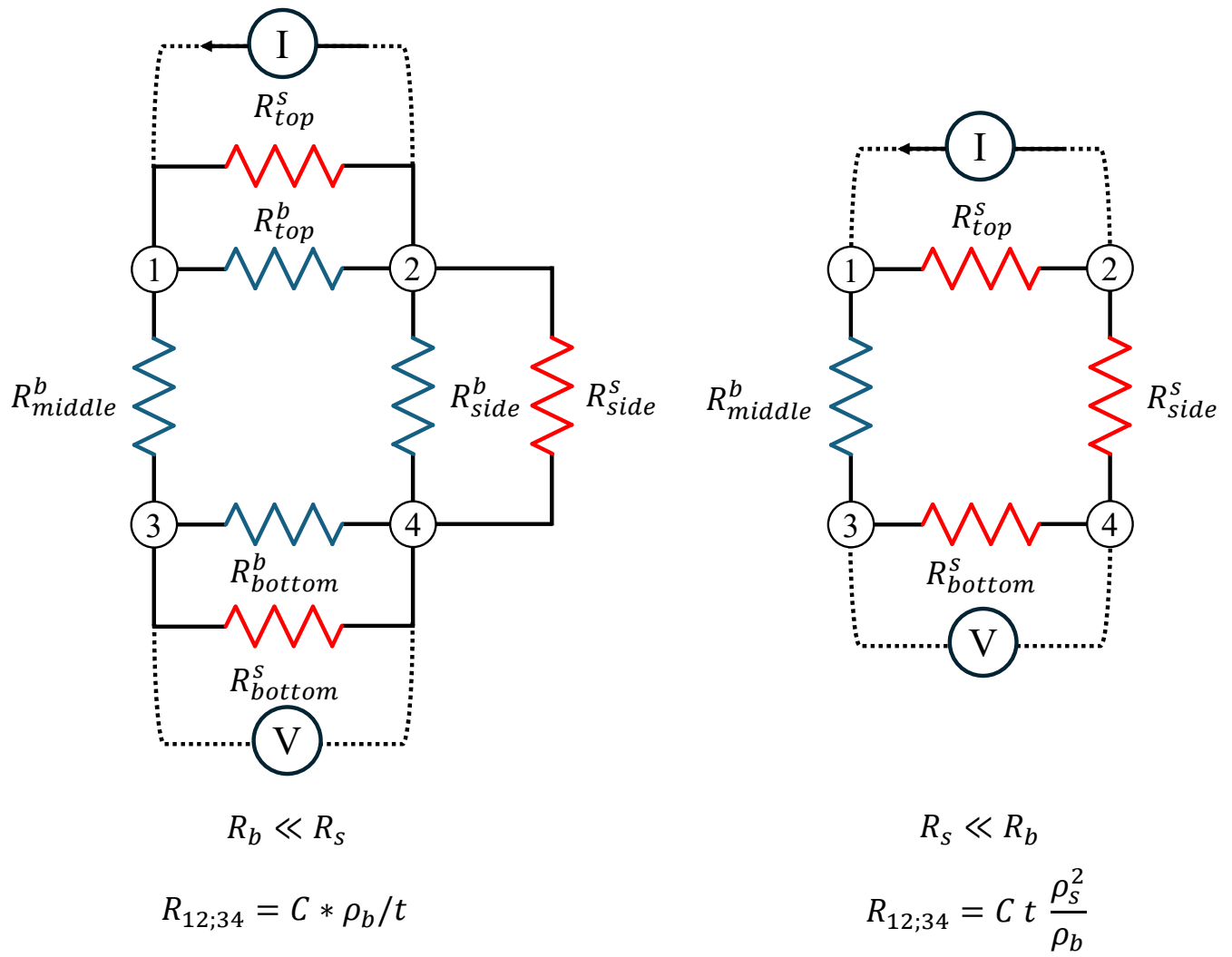


**Fig. S7. Inverted Resistance Circuit Diagram.** The effective circuit diagrams for the inverted resistance measurement.